

# Evolution of Photovoltaic Performance in Fully Printable Mesoscopic Carbon-Based Perovskite Solar Cells

Avi Schneider, Stav Alon, and Lioz Etgar\*

Hole-conductor-free carbon-based perovskite solar cells (C-PSCs) are a promising candidate for commercialization due to low cost, simple, and industry applicable fabrication methods. However, when measuring the photovoltaic parameters of these cells, they do not achieve their maximal performance immediately following their fabrication, but rather require a certain maturation period. Herein, the natural and induced changes that occur in C-PSCs are studied after their fabrication is complete. It is observed that the current density increases by natural maturation, and the open-circuit voltage increases by light-soaking treatment. Using charge extraction, intensity-modulated photovoltage spectroscopy, and voltage decay measurements during the three steps of maturation, it is possible to observe some changes in crystallization and surface traps, which are the cause for the evolution in the photovoltaic parameters. Moreover, in the case of two-step deposition, the cells achieve their final performance already as fresh cells in contrast to the case of one-step deposition cells. The conclusions offer practical information regarding the preparation and optimal measurement conditions of C-PSCs as well as possible prospects for the improvement and optimization of this cell type.

## 1. Introduction

In the rapidly progressing field of perovskite photovoltaics, with certified efficiencies exceeding 24%,<sup>[1]</sup> porous carbon-based perovskite solar cells (C-PSCs) show much promise as candidates for commercialization due to low cost, simple, and industry applicable fabrication methods.<sup>[2]</sup> Hole-conductor-free fully printable C-PSCs were first reported by Han and co-workers.<sup>[3]</sup> The lack of a hole conductor, and use of printable carbon as a substitute for gold in the back contact, substantially reduces the main price loads of traditional PSCs. Furthermore, the chosen materials and monolithic design of the C-PSCs reportedly provide fortified protection of the perovskite absorber, resulting in exceptionally high stability for unencapsulated cells.<sup>[4]</sup> Since they were first reported in 2013, with a power conversion

efficiency (PCE) of 6.6%, C-PSCs have shown substantial improvements in performance, recently reaching up to 15.7% PCE.<sup>[3,5–7]</sup> Despite this constant progress in performance, the unique structure and the fabrication process of the C-PSC are relatively less investigated due to its ranking in the race for efficiency. Here, we choose to explore the properties and characteristics of C-PSCs in the belief that better understanding may lead to improved performance.


The final step in the preparation of a C-PSC is the deposition of perovskite. This process is carried out by drop casting a perovskite precursor solution onto the porous carbon electrode and heating it on a hotplate to evaporate the solvents and induce crystallization. With the completion of this procedure, the perovskite solar cell is ready for use, with no need for the application of a hole conductor or the patterning of a metallic electrode. When measuring the photovoltaic parameters of our cells, we observed that they do not achieve their

maximal performance immediately following their completion, but rather require a certain maturation period. The improvement in PCE can reach up to 5% in some cases. In addition to this naturally occurring maturation process, we have found that an induced light-soaking treatment may further improve cell performances. Used frequently on dye-sensitized and organic solar cells, the use of light-soaking treatments on PSCs has also been investigated, showing either reversible or irreversible effects depending on the cell composition.<sup>[8–10]</sup>

In the fabrication of C-PSCs, perovskite must form within the pores of the cell's functional layers. The complete removal of solvents from the depth of the cell might prove difficult in some cases, and various solvents and deposition conditions have been reported to address this issue.<sup>[11–14]</sup> Perovskites have been shown to possess some unusual material properties, including ion migration and self-healing.<sup>[15–19]</sup> The unique environment and fabrication conditions of the perovskite in C-PSCs, along with these peculiar attributes of the material, are likely to take part in the observed cell maturation.

In this study, we investigate the natural and induced changes that occur in C-PSCs after their fabrication is complete. In addition, we demonstrate the use of an alternative two-step perovskite deposition method and examine its influence on these post-fabrication changes in C-PSCs. The two-step deposition process, commonly used for perovskite film formation, was adapted as a substitute for the standard one-step method to form a

A. Schneider, S. Alon, Prof. L. Etgar  
The Center for Nanoscience and Nanotechnology  
Casali Center for Applied Chemistry  
The Hebrew University of Jerusalem  
Institute of Chemistry  
Jerusalem 91904, Israel  
E-mail: lioz.etgar@mail.huji.ac.il

 The ORCID identification number(s) for the author(s) of this article can be found under <https://doi.org/10.1002/ente.201900481>.

DOI: 10.1002/ente.201900481

submerged perovskite network within the pores of the C-PSC.<sup>[13]</sup> To obtain a comprehensive detailed picture of the post-fabrication evolution, we deployed a wide range of characterization techniques on the cells at the different maturation stages. Our conclusions offer practical information regarding the preparation and optimal measurement conditions of C-PSCs as well as possible prospects for the improvement and optimization of this cell type.

## 2. Results and Discussion

In this study, C-PSCs were prepared and characterized to evaluate the evolution of their photovoltaic (PV) performance following fabrication. To ensure the cells were fabricated properly and in the desired dimensions, a cross section of a completed cell was cut using a focused ion beam (FIB), and scanning electron microscope (SEM) images were taken. A cross-sectional SEM image of the cell appears in **Figure 1a**, along with an illustration of the cell architecture including a description of the functional layers (Figure 1b). The measured thicknesses of the layers in the cross section were  $\approx 1 \mu\text{m}$  each for the mesoporous titanium dioxide ( $\text{TiO}_2$ ) and zirconium dioxide ( $\text{ZrO}_2$ ) layers and  $\approx 9 \mu\text{m}$  for the porous carbon cathode.

To further assess the quality of our fabrication and the penetration of the perovskite throughout the cell, an elemental mapping of the cross section was conducted using energy dispersive X-ray spectroscopy (EDS). The EDS scan of the scaffold elements, shown in **Figure 2a**, offers a complementary labeling of the cell layers clearly visualized in the SEM image of the line scan path (Figure 2b). The spatial detection of tin, titanium, zirconium, and carbon atoms corresponds to the FTO/ $\text{TiO}_2$ / $\text{ZrO}_2$ /carbon scaffold architecture. The componential distribution picture of the cell is completed in Figure 2c, with the detection of perovskite elements iodine and lead, which are indistinguishable using only SEM imagery. The presence of I and Pb atoms throughout the entire scaffold, up to the FTO anode, indicates thorough percolation of the perovskite precursor solution. When following the distribution lines of the carbon and the perovskite elements, it is evident that the measurement strongly reflects the morphology of the cell cross section. The nearly opposite relationship seen in certain areas between the carbon and the perovskite EDS lines is indicative of the heterogeneous composition of the carbon layer,

with some parts saturated with perovskite and others completely devoid. This heterogeneity arises from the inclusion of both graphite and carbon black in the carbon paste formulation. The graphite flakes are highly dense and impenetrable by the perovskite, whereas the carbon black forms porous regions that enable the percolation of perovskite solution within the cathode and through it to the underlying layers.

### 2.1. PV Parameters and $J$ - $V$ Curves

To assess the changes occurring in the C-PSCs, we first examine the photovoltaic parameters and the current voltage ( $J$ - $V$ ) curves of the solar cells. We measured the PV performance of the prepared cells at three points in time after their fabrication was completed. The first measurement was conducted immediately following fabrication, the second measurement was done 5 days later, and the third one was performed on the 7th day, following a 1.5 h light-soaking treatment and a 12 h rest period. All cells were kept in the dark in a moisture-free nitrogen atmosphere glove box and were retrieved only for the duration of the measurements. All measurements were conducted on cells prepared using one-step and two-step deposition methods. The results show a clear trend of improvement over time and with the additional light-soaking treatment, as can be seen in the  $J$ - $V$  curves presented in **Figure 3a**. We can clearly see an increase in the current density ( $J_{sc}$ ) occurring by natural maturation, and an increase in the open circuit voltage ( $V_{oc}$ ) induced by the light-soaking treatment. When studying the trends in the average values of each PV parameter separately, we gain insight into their individual contribution to the observed changes in cell performance. Figure 3c confirms that  $J_{sc}$  of the cells is the major contributor to their natural improvement, increasing from an average value of  $15 \text{ mA cm}^{-2}$  for fresh cells to  $22 \text{ mA cm}^{-2}$  for matured cells.  $V_{oc}$ , on the other hand, is the main factor improved by the light soaking with average values rising from 0.85 V in the matured cells to 0.92 V after the treatment (Figure 3b). The fill factor (FF) of the cells appears to diminish during natural maturation but is slightly increased again by the light soaking with a total decline from 65% to 55%, as seen in Figure 3d. These trends have an overall positive effect on the average PCE of the cells, which increases from 8.3% in the fresh cells to 11.5% in the light-soaked ones (Figure 3e). When

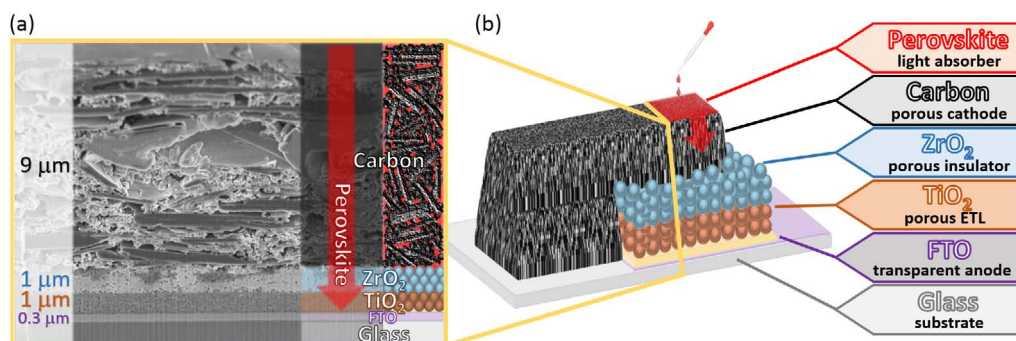


**Figure 1.** Device architecture and dimensions. a) SEM image (left) and illustration (right) of a C-PSC cross section, showing the arrangement and thickness of carbon,  $\text{ZrO}_2$ ,  $\text{TiO}_2$ , and FTO functional layers atop a glass substrate. The penetration of perovskite through the porous layers is shown in red. b) Illustration of C-PSC design. Labels on right show each layer and its function.

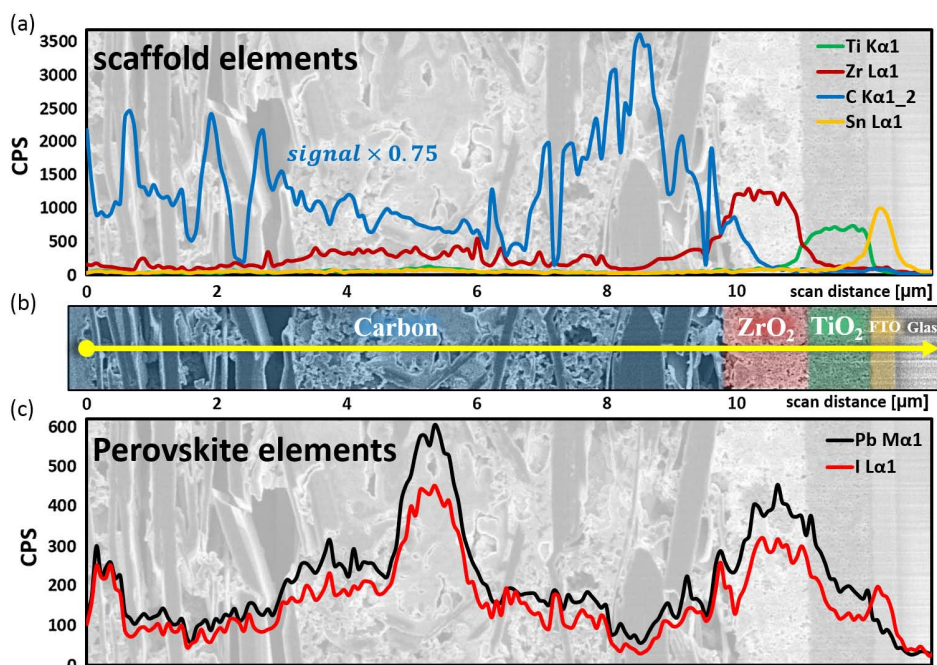


**Figure 2.** Elemental mapping of C-PSC cross section using EDS. a) Spatial distribution, in terms of counts per second, of cell scaffold elements; carbon ( $0.75 \times K\alpha_{1\_2}$ , blue), zirconium ( $L\alpha_1$ , maroon), titanium ( $K\alpha_1$ , green), and tin ( $L\alpha_1$ , yellow) along the EDS line scan of a cell cross section. Carbon signal was manually reduced to three-quarters of its original value to allow for a convenient and insightful presentation alongside the other elements b) EDS line scan path shown on an SEM image of the analyzed area, including colored shading and layer labels. c) Spatial distribution, in terms of counts per second, of perovskite elements; lead ( $M\alpha_1$ , black) and iodine ( $L\alpha_1$ , red) along the EDS line scan of a cell cross section.

comparing the cells prepared using one-step and two-step depositions, we find that the general trends are similar, but the two-step cells undergo a more moderate increase in efficiency, improving by only 1.5% compared with over 3% in the one-step cells. This difference seems to stem from the negative effect of the light soaking on  $J_{sc}$  of the two-step cells. To visualize the collective influence of these trends, we compare the  $J-V$  curves of typical one-step and two-step cells acquired at the three time points (Figure 3f–h). This perspective reveals a gradual merger of the curves obtained from each type, implying that the two-step deposition method produces cells that are initially closer to their matured optimal performance, compared with those produced with a one-step method.

## 2.2. Charge Extraction and Voltage Decay

Charge extraction (CE) measurements were conducted to acquire information about the ability of the carbon solar cells to retain charge carriers rather than lose them by recombination. The CE measurement has several stages. In the first stage, charges are generated in the cell as it is illuminated briefly in open-circuit configuration. In the second stage, the cell is left in the dark for a varying delay time until it is short circuited, and the remaining charges are extracted and quantified. A CE curve plots the amount of extracted charge against the length of the delay time before it was extracted. When comparing the CE curves of a typical cell at the three stages of maturation, a certain trend can be observed (Figure 4a). A fresh cell has the least charges to extract

for the shortest length of time, whereas in a mature cell, more charges are left to extract for the whole range of delay times, and in the case of a light-soaked cell, the charges are retained for the longest time. Under the common assumption that a longer retention of charges is beneficial to the cell, this trend is in agreement with the observed improvement in PV solar cell performance. A similar behavior is seen in cells prepared using a two-step perovskite deposition (Figure S1, Supporting Information).

CE measurements are comprised of a collection of isolated samplings, each of which producing a single data point containing the amount of charge collected and the length of the delay time. To acquire a broader picture, it is possible to focus on a single point of measurement and monitor the dynamics of the cell during the delay time. Such a measurement is called voltage decay (VD), and it follows the decline of the potential built up by the initial illumination of the cell. This VD is caused by the same loss of charges we observe in the CE measurement and is indicative of the rate of charge carrier recombination. When comparing the VD curves of the cell at different maturation stages, we see a similar trend as in CE (Figure 4b). The potential is maintained longer for matured cells compared with the fresh ones and even longer for light-soaked cells. A similar behavior is observed in two-step prepared cells (Figure S2, Supporting Information).

Interestingly, it appears that the built-in potential of both matured and light-soaked cells does not decay entirely, even after a full minute in the dark, whereas the potential of the fresh cells decays to zero within about 40 s. Similar results were observed in a previous study conducted on MAPbI<sub>3</sub> PSCs.<sup>[20]</sup> The study,

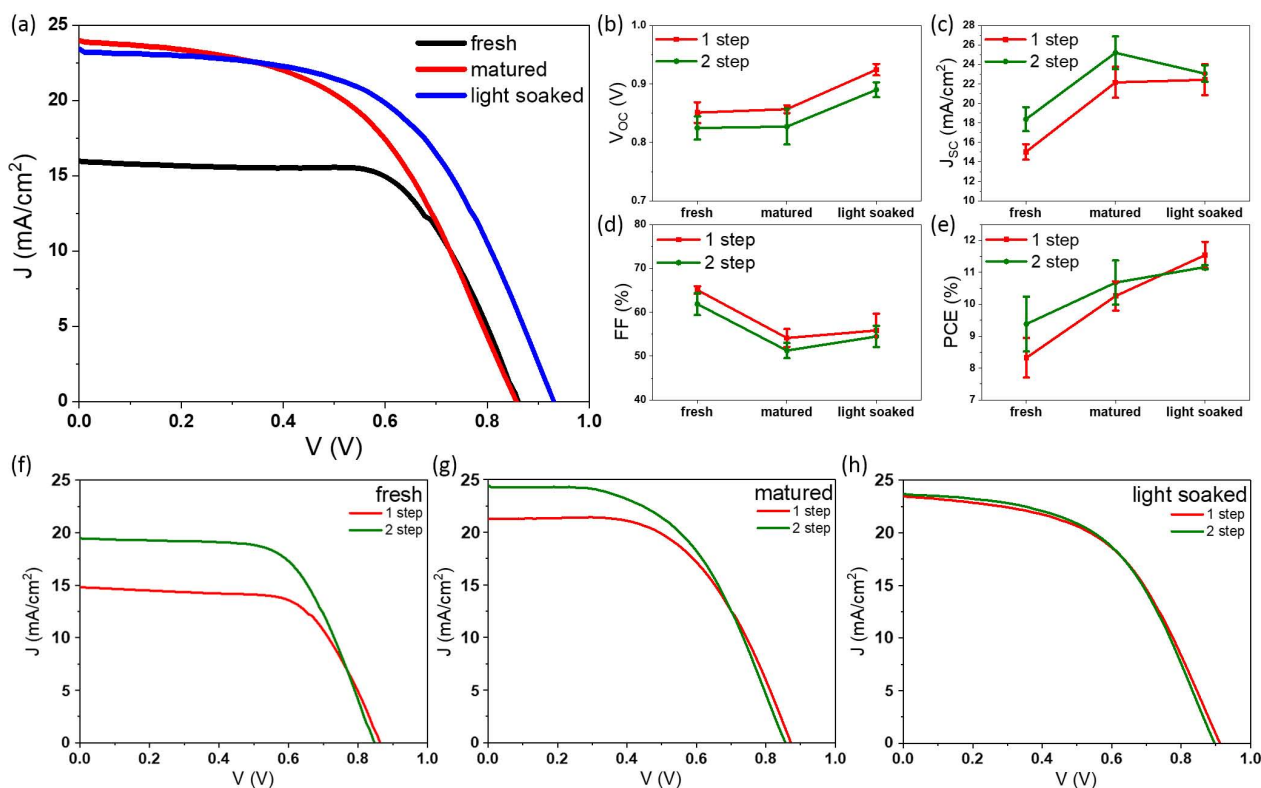


**Figure 3.** Photovoltaic characterization of post-fabrication evolution in one-step and two-step C-PSC. a) Current density versus voltage ( $J$ - $V$ ) curve of a typical C-PSC at the three measured stages of maturation; fresh (black), matured (red), and light soaked (blue). b-e) Average values of (b) open-circuit voltage ( $V_{oc}$ ), (c) short-circuit current density ( $J_{sc}$ ), (d) FF, and (e) PCE measured at the three maturation stages for cells prepared using one-step (red) and two-step (green) deposition methods. Error bars represent standard deviation of measured cells from the average. f-h)  $J$ - $V$  curves of (f) fresh, (g) matured, and (h) light-soaked C-PSCs prepared using one-step (red) and two-step (green) deposition methods.

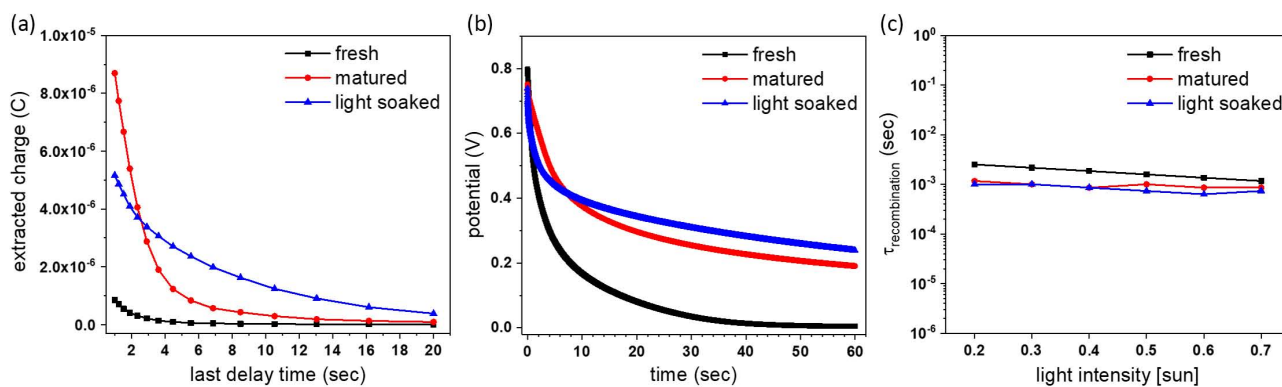


**Figure 4.** CE, VD, and IMVS measurements of post-fabrication evolution in C-PSCs. a) Values of extracted charge as a function of delay time after illumination for a typical C-PSC at the three maturation stages. b) Voltage decay measurements of a typical C-PSC at the three maturation stages. The potential of the cell is monitored over time following an initial illumination. c) Semilogarithmic plot of recombination lifetime as a function of light intensity, as calculated from IMVS measurements of a typical C-PSC at the three maturation stages.

which follows the VD behavior of cells under different illumination treatments, concluded that charge accumulation at the interface between perovskite and selective contacts induces an internal electrostatic potential. This potential, brought on by ion migration to the interfacial regions, is added on to the

photoinduced potential buildup, increasing the overall voltage of the cell.

The dominantly occurring defects in  $\text{MAPbI}_3$  create shallow trap states close to the valence band maxima and conduction band minima. Though some possible defects in the perovskite

would form mid-gap trap states, their formation energies are high and they rarely occur. Shallow trap states are less likely to act as recombination centers and may even assist in the segregation of opposite charges.<sup>[21,22]</sup> It has been proposed that shallow trap states at the selective contact interfaces may retard the recombination of charge carriers in the dark (delay time), allowing for carrier lifetimes much longer than the material's intrinsic values.<sup>[23,24]</sup> This enables free charges to survive the increasing delay time until extraction, and it is assumed to affect the vitality of charges in the working cell as well. The spatial proximity of the defect states to the perovskite-contact interface is expected to affect the tendency of trapped charges to be extracted rather than recombine. Therefore, it is speculated that the prolonged lifetime of charges in matured and light-soaked cells is related to changes in the quantity and spatial distribution of trap states, and that this may play a role in the enhanced PV performance of the cells.<sup>[8–10]</sup>

Alternatively, ion migration within the perovskite may serve as a more plausible explanation for the slower recombination rates, observed for matured and light-soaked cells in both CE and VD measurements. As aforementioned, this type of material behavior has been recorded in perovskites, and it may play a role in the observed changes in CE and cell performance.<sup>[15–17,20]</sup> An internal potential buildup caused by ion migration is expected to support a prolonged separation of charges within the perovskite and is likely to be induced by light soaking because upon illumination a potential is built up inside the cell with no means of current flow.<sup>[8–10]</sup> In addition to ion dynamics, a delayed crystallization of perovskite within the mesoporous scaffold is the cause for some additional trap states at the interfaces, effecting charge recombination. In such a scenario, some perovskite precursors may remain dissolved in trapped solvents, which undergo complete evaporation only after a few days, causing more crystals to form. This crystallization would most likely not continue throughout the life of the cell but be restricted to a short period of time ensuing fabrication. We may further discuss that the additional improvement induced by the light-soaking treatment is brought on in a similar fashion.

### 2.3. Intensity-Modulated Photovoltage Spectroscopy

We conducted additional comparative characterization of C-PSCs at the different maturation stages using intensity-modulated photovoltage spectroscopy (IMVS). This method helps gain information on the characteristic lifetimes of certain reactions occurring inside the solar cell. The most common parameter retrieved using this technique is the carrier recombination lifetime. This measurement also delivers information about the relationship between the recombination lifetime and the light intensity.

The calculated carrier recombination lifetimes at each light intensity are plotted in Figure 4c for every stage of maturation. The results show that both the natural and induced maturation processes have only a very minute diminishing effect on the carrier recombination lifetime measured using IMVS. The observed lifetimes are on the order of single microseconds, measured at a frequency range of 50–500 Hz. These carrier recombination lifetimes remain relatively constant at all light intensities. Zarazua et al.<sup>[25]</sup> reported a similar observation where the

resistivity and capacitive elements behave in opposite directions with respect to light intensity and, therefore, result in a constant time characteristic. This time characteristic can be related to surface charge accumulation at the interface.<sup>[26,27]</sup> We can predict that the constant carrier recombination lifetimes as a function of the light intensity is associated with ion migration as was also previously reported.<sup>[28]</sup> Importantly, the recombination lifetime differences between fresh, matured, and light-soaked cells, observed in the IMVS measurement, are too small to carry much significance. Furthermore, the light intensity used in the previous methods corresponds to the highest intensity used in the IMVS measurements (0.7 suns), where the differences in lifetimes are even smaller. The solar cells prepared using both the one-step deposition method and the two-step deposition method show very similar behavior in the IMVS measurements (Figure S3, Supporting Information).

### 2.4. X-Ray Diffraction Analysis

To gain insight into changes that may perhaps occur in the perovskite during the natural and induced maturation processes, we performed X-ray diffraction (XRD) measurements on complete solar cells at the three maturation stages. X-ray diffractograms contain information about crystalline structures within a sample, and in complex samples such as a complete C-PSC, many components appear together and must be properly distinguished. To differentiate between the cell components, all peaks must be assigned to particular crystal structures. As the crystal structures of all components in our solar cells are well known, peak assignment was done for SnO<sub>2</sub>, graphite, TiO<sub>2</sub>, ZrO<sub>2</sub>, PbI<sub>2</sub>, and tetragonal phase MAPbI<sub>3</sub> perovskite using the XRD crystal structure database and published literature.<sup>[29]</sup> For comparison between the cells at the different stages, we focus on the peaks assigned to the perovskite. The main graphite peaks in all diffractograms, appearing at  $2\theta$  angles of 26.7°, were manually diminished by a factor of 50 to allow for a reasonable presentation of perovskite peaks.

As can be seen in Figure 5a, the X-ray diffractograms of all three stages are virtually identical. A closer look at the main characteristic perovskite peaks offers almost no further distinction between the maturation stages. Aside from a minor increase in the peak intensity of matured and light-soaked cells compared with the fresh ones, appearing in Figure 5b,c, the three stages are practically undistinguishable when inspecting most peaks (Figure 5d–f). A peak analysis was conducted graphically, and the intensity, position, and full width at half maxima (FWHM) were compared (Table S1, Supporting Information). Based on these results, it appears that if additional crystallization occurs during maturation, it is on a very small scale. Though this scenario would correspond well with speculations made during our interpretation of the CE results, it cannot be inferred undisputedly from the XRD results, and therefore, does not seem substantial enough to account for all the changes occurring throughout the evolution of the cells. It is likely that if this late crystallization occurs, it contributes only partially to the significant improvement of the C-PSCs.

In addition to the information it delivers regarding the maturation processes, the XRD measurement provides us with

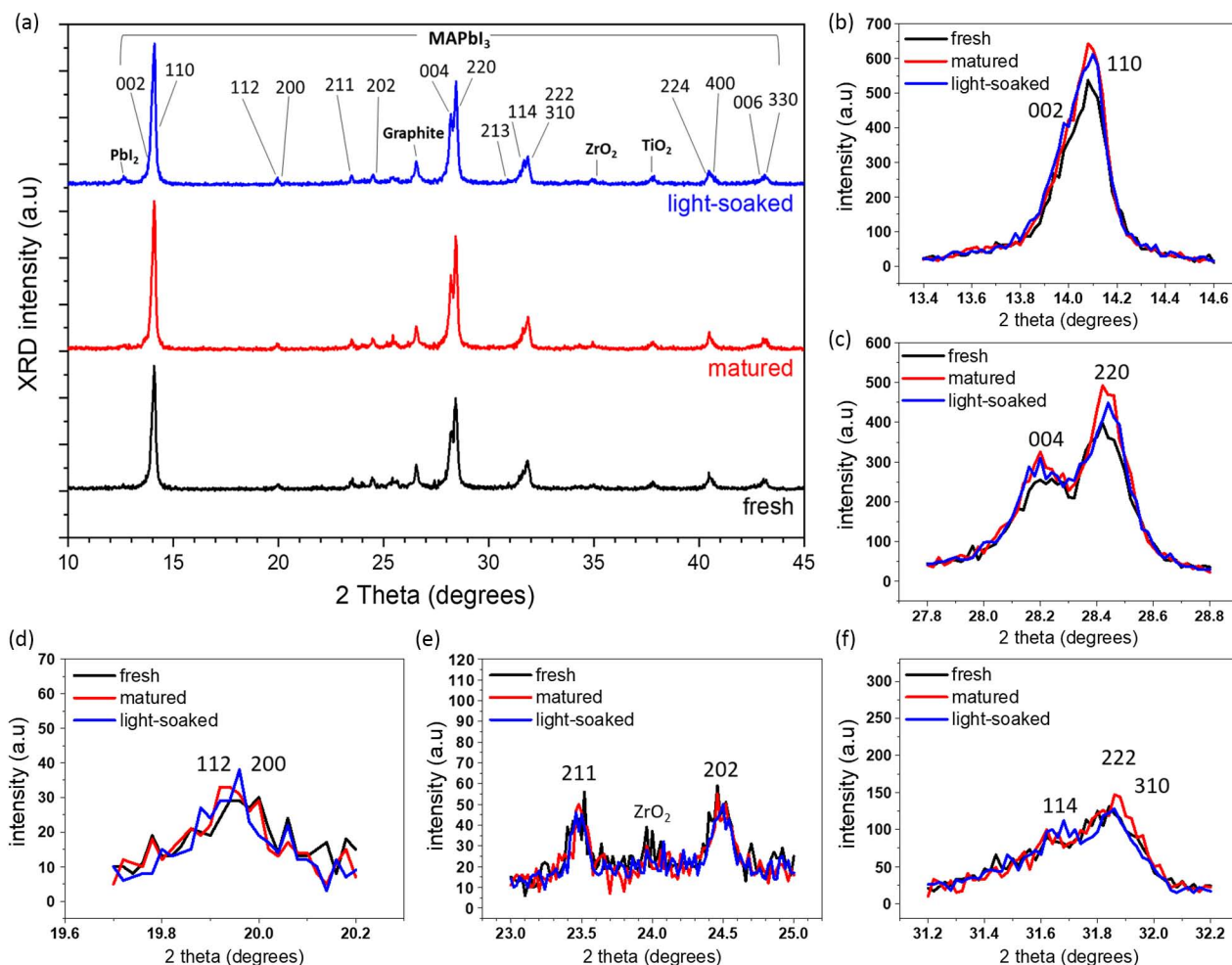


**Figure 5.** XRD measurements of post-fabrication evolution in C-PSCs. a) X-ray diffractogram of typical C-PSCs at the three maturation stages. Assigned peaks for graphite, TiO<sub>2</sub>, ZrO<sub>2</sub>, Pbl<sub>2</sub>, and multiple planes of tetragonal CH<sub>3</sub>NH<sub>3</sub>PbI<sub>3</sub> (MAPbI<sub>3</sub>) perovskite are indicated on the diffractogram of the light-soaked cell but refer to all measurements. The main graphite peak (26.7°) was manually diminished 50-fold to allow reasonable presentation of perovskite peaks. FTO peaks were also assigned but do not appear on the diffractogram. b–f) Magnification of the diffractograms of the three maturation stages at regions of interest focusing on the (b) <002> and <110>, (c) <004> and <220>, (d) <112> and <200>, (e) <221> and <202>, and (f) <114>, <222>, and <310> facets of tetragonal MAPbI<sub>3</sub> perovskite.

some insight into the nature of the differences observed between one-step and two-step deposition methods. When comparing the X-ray diffractograms of cells prepared by each method, we can see that certain differences appear consistently, no matter what stage of maturation the cells are in. A representative comparison between the diffractograms of matured one-step and two-step cells is shown in **Figure 6a**. Apart from the noticeable appearance of the tetragonal <213> facet peak in the two-step solar cell, it is difficult to observe and quantify differences at this resolution; therefore, a precise analysis of the relevant peaks is used (Table S2, Supporting Information).

To visually compare the peaks of the one and two-step cells, we use magnifications of the same characteristic perovskite peaks we evaluated when inspecting the cell evolution. The lowest angle perovskite peak, appearing at a  $2\theta$  angle of  $\approx 14.1^\circ$ , is, in fact, comprised of two adjacent peaks assigned to the tetragonal <002> and <110> facets (Figure 6b). This peak appears quite

similar in the one-step and two-step cells with a slightly narrower peak for the two-step cells and a very minor upward shift of the angle. A better understanding of these differences is gained by looking at parallel planes with half the  $d$  spacing (double the Miller indices). In this case, we look at the <004> and <220> facets appearing at  $2\theta$  angles of  $28.2^\circ$  and  $28.4^\circ$ , respectively (Figure 6c). Here, we see that the <004> peak of the one-step cell is much more intense than the equivalent peak of the two-step cell, and the <220> peak is only slightly more intense than that of the two-step cell. If we use this information to interpret the  $14.1^\circ$  peak as well, we can assume that there is a more prominent contribution from the <002> facet in the case of the one-step cell. Combined with the <110> facet signal, a broader peak is formed, centered in between the precise angles of these facets. The same peak in the two-step cell is mostly comprised of the <110> facet and not the <002> facet, and it is, therefore, narrower and centered around the <110> facet angle.

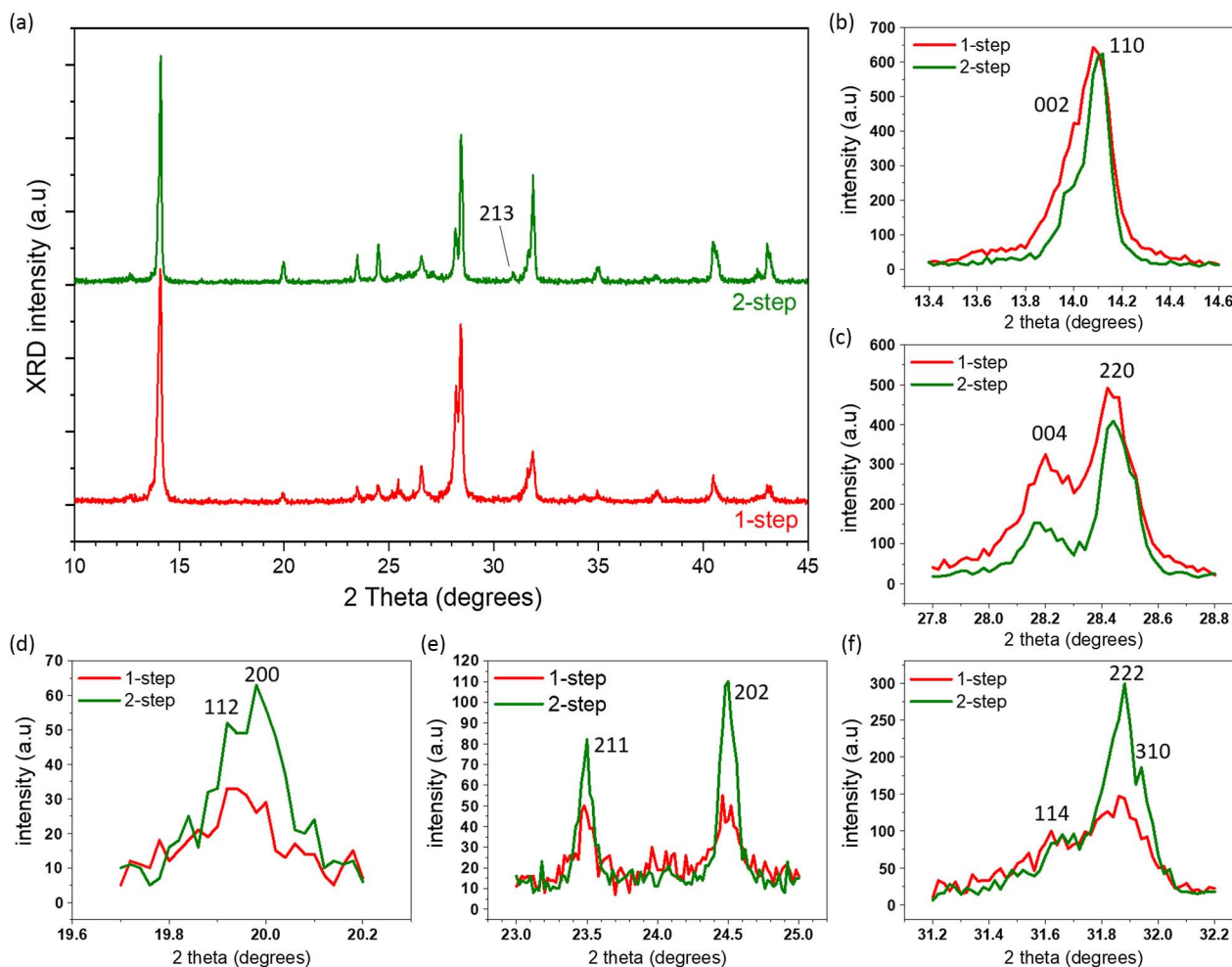


**Figure 6.** XRD measurements of C-PSCs prepared using one-step and two-step deposition methods. a) X-ray diffractogram of matured C-PSCs prepared using one-step (red) and two-step (green) deposition. Peak assignment is not indicated but is identical to the one in Figure 5a. The peak of tetragonal MAPbI<sub>3</sub> facet <213> is indicated to highlight its appearance. The main graphite peak (26.7°) was manually diminished 50-fold to allow reasonable presentation of perovskite peaks. b–f) Magnification of the diffractograms of the one-step (red) and two-step (green) cells at regions of interest focusing on the (b) <002> and <110>, (c) <004> and <220>, (d) <112> and <200>, (e) <211> and <202>, and (f) <114>, <222>, and <310> facets of tetragonal MAPbI<sub>3</sub> perovskite.

Another point of difference between the one- and two-step cells is seen at a  $2\theta$  angle of  $\approx 19.9^\circ$ . This peak is also formed by the fusing of two neighboring peaks, belonging to the <112> and <200> facets (Figure 6d). In this case, it is clear to see that the peak of the two-step cell has a higher intensity than that of the one-step cell. The same can be seen when examining the <211> and <202> facet peaks in Figure 6e, the <213> facet peak in Figure 6a, and the <222> and <310> facet peaks in Figure 6f.

These differences suggest that there is a preference in either the direction or the orientation of perovskite crystal growth in the two-step cells. We conducted our XRD measurements on complete solar cells using powder XRD instrumentation and diagnostic tools. If the perovskite crystals in the cell are formed with a certain preferred orientation rather than in completely random orientations, as required for powder XRD, we are expected to measure intensities that are not necessarily an adequate

representation of the measured perovskite. On the other hand, particular deposition methods have been shown to induce a certain extent of anisotropic crystal growth,<sup>[12]</sup> thereby enhancing the signals of specific facets and not others. One thing is clear from the XRD results that the perovskites created by one-step and two-step depositions are not necessarily identical. It is, therefore, not surprising that the two methods produce solar cells of different qualities, with dissimilar trends in maturation.

### 3. Conclusions

In this study, we have elucidated the processes occurring in C-PSCs after their fabrication is complete, both naturally and in response to a light-soaking treatment. It was found that, for matured cells, the current density increases compared with the fresh cells, whereas the open circuit voltage increases for

light-soaked cells. On the whole, it is clear that the fresh PV performance of the C-PSC is not the optimal, and both matured and light-soaked cells show improved performance. We additionally studied the use of an adapted two-step perovskite deposition method as an alternative to the traditional one-step method, and we characterized some of the differences between cells prepared in either way. Our results indicate that during natural and induced maturation, carbon-based perovskite solar cells undergo changes that may affect the carrier recombination processes in the cell, thereby improving its performance. Part of the changes are related to delayed crystallization of the perovskite within the cell, though evidence of it is scarce, whereas others are more likely to have been brought on by ionic rearrangement within it. XRD measurements imply that perovskites in the one-step and two-step cells differ at a crystalline level, explaining the slightly different trends each cell type displays during maturation. This work sheds light on the dynamic nature of the carbon-based perovskite solar cell and offers some findings that may be instrumental in the optimization of this cell type. Further research into the two-step method and other deposition conditions may provide the advancement needed to make C-PSCs a truly competitive technology.

## 4. Experimental Section

**Materials and Solvents:** Hellmanex III, titanium diisopropoxide bis(acetylacetonate) (75 wt% in isopropanol), lead iodide (99%), *N,N*-dimethylformamide (DMF, anhydrous 99.8%), and isopropyl alcohol (IPA, anhydrous 99.5%) were purchased from Sigma-Aldrich. Methylammonium iodide (MAI) and TiO<sub>2</sub> paste (90T) were purchased from GreatCell Solar Company. Zr-Nanoxide ZT/SP (46411) was purchased from Solaronix. Titanium (IV) chloride (TiCl<sub>4</sub>) was purchased from Wako. Ethanol absolute (99.5%) and dimethyl sulfoxide (DMSO, 99.7% Extra dry) were purchased from Acros Organics. A hyperthermic conductive carbon paste was purchased from FEIMING Chemical Ltd. All perovskite precursors and anhydrous solvents were kept in a nitrogen-filled glove box and used as received.

**C-PSC Scaffold Preparation:** Fluorine-doped tin oxide (FTO) coated glass slides were laser etched to segregate anodal and cathodal sections of the cell. The slides were then cleaned thoroughly, first by hand and then in an ultrasonic bath—three cycles of 15 min in soap, Hellmanex 1%, and deionized water. The dried substrates were then treated under argon plasma for 10 min. Next, the slides were spin-coated with a 13.3% solution of titanium diisopropoxide bis(acetylacetonate) in ethanol (5000 rpm, 30 s) and annealed on a hotplate (30 min, 450 °C). After cooling down, the substrates were immersed in a water-based TiCl<sub>4</sub> solution (1.6 mL TiCl<sub>4</sub>, 150 mL TDW) and placed in an oven at 70 °C for 30 min. Immediately after, the slides were dried and annealed at 450 °C for 30 min. Next, the successive application of TiO<sub>2</sub>, ZrO<sub>2</sub>, and carbon layers was commenced. The application of all three porous layers was executed similarly via screen printing and sintering on a hotplate. TiO<sub>2</sub> paste and ZrO<sub>2</sub> paste were screen printed using a 120-mesh polymer screen, whereas carbon paste was printed using a 45-mesh polymer screen. After the printing of each porous layer, the substrates were sintered on a hotplate for 30 min at 500 °C. Between the printing of the TiO<sub>2</sub> and ZrO<sub>2</sub> layers, a second round of the aforementioned TiCl<sub>4</sub> treatment was conducted on the substrates.

**Perovskite Solution Preparation, One-Step and Two-Step Deposition:** The completed scaffolds were placed in a nitrogen-filled no-humidity glove box for the perovskite deposition process or for storage and deposition at a later time. For one-step deposition, a 1 M solution of MAPbI<sub>3</sub> was prepared by mixing 0.461 g PbI<sub>2</sub> powder and 0.159 g MAI powder in an 85:15 ratio of DMF and DMSO, respectively. For two-step deposition, a 2 M solution of PbI<sub>2</sub> was prepared using the same solvent mixture as for the one-step solution, and a 0.06 M solution of MAI in IPA was also prepared. Before

deposition, the cells were heated on a hotplate to 200 °C for 30 min to insure the expulsion of any adsorbed humidity within the porous scaffold. After cooling, either a one-step or two-step deposition was performed. For one-step deposition, 3 μL of the MAPbI<sub>3</sub> solution was cast onto the center of the porous carbon electrode, allowed to filtrate for 1 min, and then annealed on a hotplate at 100 °C for 30 min. For two-step deposition, 3 μL of the PbI<sub>2</sub> solution was cast onto the center of the porous carbon electrode, allowed to filtrate for 5 min, and then annealed on a hotplate at 100 °C for 30 min. The substrates were then immersed in the MAI solution for 20 min, dipped in clean IPA for 5 s, and annealed on a hotplate for 30 min at 70 °C. For the characterizations, six cells were prepared using a one-step deposition, and three cells were prepared using a two-step deposition.

**SEM, FIB, and EDS:** To obtain a high-quality cross section of the cell for SEM imagery and EDS analysis, a sample was placed inside a FEI Helios NanoLab 460F1 and excavated using a focused gallium ion beam to expose the layered structure. The layered stack was imaged and measured, and a slab was retrieved and placed on a separate holder to enable a 90° EDS line scan. The EDS scan was conducted using electron beam energies between 5 and 30 kV to identify the desired elements.

**PV Characterization:** Current–voltage curves and standard photovoltaic properties were obtained using a Newport solar simulator system consisting of an Oriel *I*–*V* test station with an Oriel Sol3A simulator. The solar simulator was Class AAA for spectral performance, uniformity of irradiance, and temporal stability. It was equipped with a 450 W xenon lamp. The output power was adjusted to match AM1.5 global sunlight (100 mW cm<sup>-2</sup>). The spectral match classifications were IEC60904-9 2007, JIC C 8912, and ASTM E927-05. *I*–*V* curves were obtained by applying a varying external bias to the cell and measuring the generated photocurrent with a Keithley model 2400 digital source meter. The bias voltage was scanned from 1 to –0.1 V in steps of 10 mV with a dwell time of 40 ms at each step. Photovoltaic performance was measured using an opaque mask with an aperture area of 0.085 cm<sup>2</sup> (measured using an optical caliper). A silicon reference cell was used to calibrate the solar simulator. All PV measurements were carried out under ambient conditions in air (temperature of 25 ± 3 °C and humidity 40% ± 10%).

**Charge Extraction, Voltage Decay, and IMVS:** CE, VD, and IMVS were measured using Autolab Potentiostat-Galvanostat (PGSTAT) with a FRA32M LED driver equipped with a cool white light source. A Nova 2.1 software program was used to collect and analyze the obtained data. The CE measurement parameters used were as follows—discharge time of 2 s, illumination time of 5 s, and delay times measured were 1, 1.2, 1.5, 1.9, 2.3, 2.9, 3.6, 4.4, 5.5, 6.8, 8.5, 10.5, 13, 16.1, and 20 s. The VD measurements followed the decay of the photoinduced potential in the cell over a period of 60 s, following a 5 s illumination. The IMVS measurements were conducted by illuminating the sample at different light intensities, varying from 0.2 to 0.7 sun, with a sinusoidal wave modulation, with frequencies ranging from 1 Hz to 50 kHz. Lifetimes were calculated using the formula:  $\tau = 1/(2\pi \cdot \text{frequency at minimum of semicircle})$ .

**XRD:** Powder XRD measurements were performed on complete C-PSCs at the different maturation stages using a D8 Advance diffractometer (Bruker AXS, Karlsruhe, Germany). The diffractometer was operated in grazing incidence X-ray diffraction (GIXRD) mode with a grazing incidence angle value of 2.5°. The diffractometer was equipped with a 217.5 mm radius goniometer, a secondary graphite monochromator, 2° Soller slits, and a 0.2 mm receiving slit. XRD patterns were recorded using Cu K $\alpha$  radiation (1 1/4 1.5418 Å) with a tube voltage of 40 kV and a tube current of 40 mA. A step-scan mode was used with a step size of 0.02° 2 $\theta$ , and a counting time of between 1 and 3 s per step. Measurements were conducted at room temperature.

## Supporting Information

Supporting Information is available from the Wiley Online Library or from the author.



## Acknowledgements

This work was supported by the Israel-China (ISF-NSFC) program grant number 2552/17 and by the Israel Science foundation grant number 937/18.

## Conflict of Interest

The authors declare no conflict of interest.

## Keywords

light soaking, mesoscopic carbon solar cells, perovskites, photovoltaics

Received: April 28, 2019

Published online:

- 
- [1] NREL PV chart, <https://www.nrel.gov/pv/assets/pdfs/best-research-cell-efficiencies-190416.pdf> (accessed: May 2019).
- [2] Y. Rong, Y. Hu, A. Mei, H. Tan, M. I. Saidaminov, S. Il Seok, M. D. McGehee, E. H. Sargent, H. Han, *Science* **2018**, 361, eaat8235.
- [3] Z. Ku, Y. Rong, M. Xu, T. Liu, H. Han, *Sci. Rep.* **2013**, 3, 3132.
- [4] X. Li, M. Tschumi, H. Han, S. S. Babkair, R. A. Alzubaydi, A. A. Ansari, S. S. Habib, M. K. Nazeeruddin, S. M. Zakeeruddin, M. Grätzel, *Energy Technol.* **2015**, 3, 551.
- [5] A. Mei, X. Li, L. Liu, Z. Ku, T. Liu, Y. Rong, M. Xu, M. Hu, J. Chen, Y. Yang, M. Grätzel, H. Han, *Science* **2014**, 345, 295.
- [6] P. Jiang, T. W. Jones, N. W. Duffy, K. F. Anderson, R. Bennett, M. Grigore, P. Marvig, Y. Xiong, T. Liu, Y. Sheng, L. Hong, *Carbon N. Y.* **2018**, 129, 830.
- [7] C. Tian, A. Mei, S. Zhang, H. Tian, S. Liu, F. Qin, Y. Xiong, Y. Rong, Y. Hu, Y. Zhou, S. Xie, *Nano Energy* **2018**, 53, 160.
- [8] C. Zhao, B. Chen, X. Qiao, L. Luan, K. Lu, B. Hu, *Adv. Energy Mater.* **2015**, 5, 1.
- [9] S. Shao, M. Abdu-Aguye, L. Qiu, L. H. Lai, J. Liu, S. Adjokatsé, F. Jahani, M. E. Kamminga, G. H. Ten Brink, T. T. M. Palstra, B. J. Kooi, *Energy Environ. Sci.* **2016**, 9, 2444.
- [10] C. Liu, J. Fan, X. Zhang, Y. Shen, L. Yang, Y. Mai, *ACS Appl. Mater. Interfaces* **2015**, 7, 9066.
- [11] C. Y. Chan, Y. Wang, G. W. Wu, E. Wei-Guang Diau, *J. Mater. Chem. A* **2016**, 4, 3872.
- [12] C. M. Tsai, G. W. Wu, S. Narra, H. M. Chang, N. Mohanta, H. P. Wu, C. L. Wang, E. W. G. Diau, *J. Mater. Chem. A* **2017**, 5, 739.
- [13] T. Liu, L. Liu, M. Hu, Y. Yang, L. Zhang, A. Mei, H. Han, *J. Power Sources* **2015**, 293, 533.
- [14] S. G. Hashmi, D. Martineau, M. I. Dar, T. T. T. Myllymäki, T. Sarikka, V. Ulla, S. M. Zakeeruddin, M. Grätzel, *J. Mater. Chem. A* **2017**, 5, 12060.
- [15] Y. Yuan, J. Huang, *Acc. Chem. Res.* **2016**, 49, 286.
- [16] Y. Shao, Y. Fang, T. Li, Q. Wang, Q. Dong, Y. Deng, Y. Yuan, H. Wei, M. Wang, A. Gruverman, J. Shield, *Energy Environ. Sci.* **2016**, 9, 1752.
- [17] C. Eames, J. M. Frost, P. R. F. Barnes, B. C. O'Regan, A. Walsh, M. S. Islam, *Nat. Commun.* **2015**, 6, 2.
- [18] W. Nie, J. C. Blancon, A. J. Neukirch, K. Appavoo, H. Tsai, M. Chhowalla, M. A. Alam, M. Y. Sfeir, C. Katan, J. Even, S. Tretiak, *Nat. Commun.* **2016**, 7, 1.
- [19] F. Lang, N. H. Nickel, J. Bundesmann, S. Seidel, A. Denker, S. Albrecht, V. V. Brus, J. Rappich, B. Rech, G. Landi, H. C. Neitzert, *Adv. Mater.* **2016**, 28, 8726.
- [20] R. Gottesman, P. Lopez-Varo, L. Gouda, J. A. Jimenez-Tejada, J. Hu, S. Tirosh, A. Zaban, J. Bisquert, *Chem* **2016**, 1, 776.
- [21] D. Meggiolaro, S. G. Motti, E. Mosconi, A. J. Barker, J. Ball, C. Andrea Riccardo Perini, F. Deschler, A. Petrozza, F. De Angelis, *Energy Environ. Sci.* **2018**, 11, 702.
- [22] W.-J. Yin, T. Shi, Y. Yan, *Appl. Phys. Lett.* **2014**, 104, 063903.
- [23] N. W. Duffy, L. M. Peter, R. M. G. Rajapakse, K. G. U. Wijayantha, *Electrochem. Commun.* **2000**, 2, 658.
- [24] X. Wu, M. T. Trinh, D. Niesner, H. Zhu, Z. Norman, J. S. Owen, O. Yaffe, B. J. Kudisch, X. Y. Zhu, *J. Am. Chem. Soc.* **2015**, 137, 2089.
- [25] I. Zarazua, G. Han, P. P. Boix, S. Mhaisalkar, F. Fabregat-Santiago, I. Mora-Seró, J. Bisquert, G. Garcia-Belmonte, *J. Phys. Chem. Lett.* **2016**, 7, 5105.
- [26] O. Almora, I. Zarazua, E. Mas-Marza, I. Mora-Sero, J. Bisquert, G. Garcia-Belmonte, *J. Phys. Chem. Lett.* **2015**, 6, 1645.
- [27] E. J. Juarez-Perez, R. S. Sanchez, L. Badia, G. Garcia-Belmonte, Y. S. Kang, I. Mora-Sero, J. Bisquert, *J. Phys. Chem. Lett.* **2014**, 5, 2390.
- [28] T. Y. Yang, G. Gregori, N. Pellet, M. Grätzel, J. Maier, *Angew. Chem., Int. Ed.* **2015**, 54, 7905.
- [29] T. Baikie, Y. Fang, J. M. Kadro, M. Schreyer, F. Wei, S. G. Mhaisalkar, M. Graetzel, T. J. White, *J. Mater. Chem. A* **2013**, 1, 5628.